REGULAR PAPER

Development of a Three-Dimensional Ultrasonic Elliptical Vibration Transducer (3D-UEVT) Based on Sandwiched Piezoelectric Actuator for Micro-grooving

Rendi Kurniawan[1] · Saood Ali[1] · Ki Moon Park[1] · Chang Ping Li[2] · Tae Jo Ko[1,2]

Abstract
A three-dimensional ultrasonic elliptical vibration transducer (3D-UEVT) based on a sandwiched piezoelectric actuator for micro-grooving was manufactured and assessed in this study. The 3D-UEVT generates an elliptical locus of a tool tip in three-dimensional space. The 3D-UEVT operates in resonance mode by coupling the first longitudinal-vibration mode and the two directions of the third bending-vibration mode. Modal simulation analysis was performed to determine the proper dimensions to ensure that the resonance frequencies between the longitudinal and two of the bending-vibration modes were similar. The swept-sine assessment indicated that the 3D-UEVT working resonance frequency was approximately 20.4 kHz. The 3D-UEVT generated an amplitude peak-to-peak of approximately 0.8 μm in two-bending directions and 0.3 to 0.5 μm in the longitudinal direction when the piezoelectric sandwiched actuator was driven at a peak-to-peak voltage of 150 V. The output amplitude of the 3D-UEVT increased as the driven input voltage increased. The performance of the proposed 3D-UEVT was assessed by a micro-grooving test. An adequate micro-grooving result confirmed that the proposed 3D-UEVT produced an acceptable micro-groove pattern.

Keywords PZT · Elliptical vibration · Piezoelectric · Ultrasonic transducer · Modal analysis

1 Introduction

There has been a gradual development of the elliptical vibration transducer since Moriwaki et al. introduced the elliptical vibration cutting (EVC) method [1, 2]. There has been a recent change, from non-resonance to resonance, in the design of the elliptical vibration transducer [3]. Further, the piezo actuator arrangement has been modified (parallel [4], perpendicular [5], or angled [6]) and a single actuator has been used [7]. The modified horn shape was implemented for the single actuator [8], and three piezo actuators were used to generate the elliptical trajectory in three-dimensional space [9]. In general, a piezo actuator is used as the main actuator in elliptical vibration transducers because it offers a quick response (no lag) [10], no friction, and adequate thermal resistance.

In recent developments, ultrasonic elliptical vibration transducers (UEVT) have been operated in a resonance condition with the coupling of two different vibration modes with similar frequencies, such as a longitudinal–longitudinal [3], longitudinal–bending [11], or bending–bending [12] vibration-coupling mode. In general, full- or half-shape piezoelectric ceramics are required to vibrate the transducer in the longitudinal (full-shape) or bending (half-shape) vibration mode [11, 12]. Piezoelectric ceramics are driven in normal polarization for the longitudinal-vibration mode. For the bending-vibration mode, reverse polarization of the half-shape of the piezoelectric ceramics is required to sequentially vibrate owing to the piezo-electrical effect in a different polarity (compression or contraction) [11]. Further, phase shift control is used to manipulate the shape of the elliptical trajectory.

✉ Rendi Kurniawan
rendi@ynu.ac.kr

✉ Tae Jo Ko
tjko@yu.ac.kr

1   School of Mechanical Engineering, Yeungnam University, 214-1, Dae-dong, Gyeongsan-si, Gyeongsangbuk-do 712-749, South Korea

2   College of Mechanical and Electrical Engineering, Hunan University of Science and Technology, Taoyuan Road, Xiangtan, Hunan, China

Moriwaki et al. [13] developed the first UEVT where the piezoelectric plates were located on the four surfaces of a square beam. The sinusoidal voltages with a proper phase shift vibrated the piezoelectric plates to excite the bending–bending vibration-coupling mode. The Moriwaki transducer could generate an elliptical amplitude of 4 μm at a working frequency of 20 kHz [13]. Beihang University developed a UEVT with a single excitation in the longitudinal direction, where the bending-vibration mode was coupled owing to the asymmetric design of the transducer [7]. The UEVT developed by Beihang University produced an elliptical amplitude of approximately 16 μm in the tangential direction and 2 μm in the normal direction with a working frequency of 22.5 kHz. The piezoelectric ceramics were perpendicularly arranged to generate an elliptical vibration at a high frequency of approximately 18 kHz, and the transducer could produce an elliptical trajectory of approximately 2 μm in the major axis direction and 1 μm in the minor axis direction [14]. Taga Electric Co., Ltd. manufactures a commercial UEVT (EL-50). The EL-50 can produce an elliptical vibration amplitude of approximately 4 μm at 39 kHz [15]. Guo et al. [3] proposed a UEVT that could generate an elliptical locus with major and minor axes of 8.79 and 7.28 μm, respectively, at a working frequency of 28 kHz. The Guo UEVT design is based on the longitudinal–longitudinal vibration-coupling mode of two angled Langevin transducers at a 60° angle [3]. Zhou et al. [11] proposed a UEVT that used a longitudinal–bending vibration-coupling mode. In principle, the first longitudinal-vibration mode has a similar frequency to that of the third bending-vibration mode [11]. The Zhou transducer had a working frequency of approximately 20.1 kHz, and the device generated an amplitude of approximately 10 μm and 8 μm in the radial and axial directions, respectively, at a high voltage of 450 V [11]. Yin et al. [8] developed a UEVT that uses a single driven piezoelectric actuator. An additional motion was added by adding an oblique beam in front of the horn [8]. The Yin transducer could generate vibration amplitudes of 10 and 3 μm in the y- and x-directions, respectively, at 20.1 kHz [8]. Huang et al. [12] proposed a UEVT that uses the principle of the bending–bending vibration-coupling mode. The Huang transducer operates at approximately 19.3 kHz and generates an elliptical locus with amplitudes in the y- and z-directions of approximately 3.5 μm at 250 V.

Numerous ultrasonic transducers with different shape variations and arrangements create an elliptical motion; however, there are minimal existing transducers that produce three-dimensional (3D) motion of an elliptical locus in the ultrasonic condition (≥ 20 kHz). Kurosawa et al. [16] proposed an ultrasonic transducer that consisted of a 90° alignment between two Langevin transducers. The Kurosawa transducer generated elliptical motion of the tip of approximately 51.6 and 9.05 μm in the tangential and

normal directions at a working frequency of 30.78 kHz [16]. Liu et al. [17] developed an ultrasonic transducer using the longitudinal–bending vibration-coupling mode. The longitudinal- and bending-mode frequencies were investigated experimentally at 28.897 kHz. The symmetrical shape of the conical horn in the Liu transducer produced a longitudinal–bending vibration-coupling mode that could synchronously create a two-dimensional motion of the feet [17]. Full- and half-shaped piezoelectric ceramics are typically used to generate the longitudinal and bending-vibration modes, respectively [18]. Yan et al. [19] proposed an ultrasonic transducer that operates in a bending–bending vibration-coupling mode, where the two different groups of piezoelectric ceramics are attached on the beam surface. Inspired by the Guo transducer, the Kurniawan transducer operates at 24 kHz with a small vibration amplitude for surface texturing applications [20, 21]. This study was inspired by Lotfi and Amini [22], who proposed a 3D-UEVT that operates at a frequency of 20 kHz.

According to Lin's report [23], the generated surface roughness by the 3D-EVC method is less than that of the 2D-EVC method. However, a contradictory result was obtained in the Sajjady report [24], where the generated surface roughness from the 3D-EVC method was greater than that of the 2D-EVC method. To study the generated surface roughness from the 3D-EVC method, in particular micro-grooving, a novel design of the 3D-UEVT is proposed. The main objective of this study is to introduce a novel 3D-UEVT with a transducer capable of ultrasonically vibrating the tool tip in 3D-dimensional space in a resonance mode by adopting longitudinal–bending bending-vibration modes. The details of the UEVT design, design analysis, and dynamic performance of the design are presented in this study.

2 Structure of the 3D-UEVT

Figure 1a displays a cross-sectional view of the proposed 3D-UEVT. Figure 1b is an isometric view of the proposed 3D-UEVT including the polarization of the PZT ceramics for the longitudinal and bending modes. The 3D-UEVT consists of a conical horn, conical back mass, reload bolt, steel plate, insulator, and PZT ceramics (full and a half), as indicated in Fig. 1. The conical horn was made of a titanium alloy (Ti–6Al–4V). The conical back mass and preload bolt were made of stainless steel (AISI 304). The type of PZT ceramic used was SS44, and the steel plate was made of AISI4340. The insulator was made of polytetrafluoroethylene (PTFE). The material properties of the conical horn, back mass, and PZT ceramics are listed in Table 1. The conical shape of the horn was chosen to magnify the vibration amplitude and velocity. The preload bolt was used to tighten the conical horn, PZT
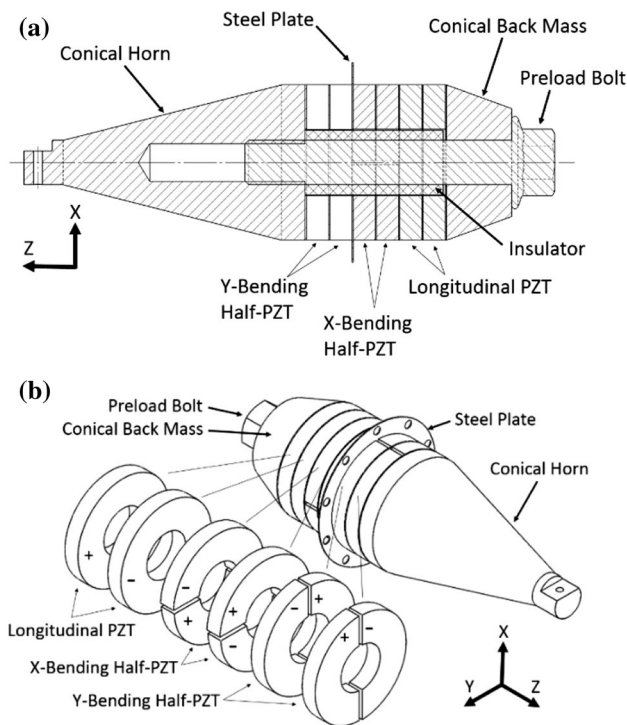
Fig. 1 Structure of proposed 3D-UEVT: **a** cross-sectional view and **b** isometric view [25]

Table 1 Material properties of the main components of 3D-UEVT

No.	Materials	Young's modulus (E) (Pa)	Mass density (ρ) (kg/m³)	Poisson's ratio (ε)
1.	PZT-SS44	8×10^{10}	7700	0.32
2.	AISI 304	1.9×10^{11}	8000	0.29
3.	Ti–6Al–4V	1.05×10^{11}	4430	0.31
4.	Brass	1×10^{11}	8500	0.33
5.	PTFE	0.5×10^{9}	2320	0.46

ceramics, and conical back mass, as indicated in Fig. 1a. The conical shape of the back mass was chosen to create a similar resonance frequency for the two directions of the third bending mode. The brass electrodes were utilized to supply the electrical energy and were located between the two PZT ceramics, although the brass electrode was drawn as a circular plate, as depicted in Fig. 1. The PZT ceramics were manufactured by the SunnyTec Company. The anisotropic PZT properties: piezoelectric charge, compliant, and dielectric constants, are given by Eqs. (1)–(3), respectively.

$$\mathbf{d} = \begin{bmatrix} 0.0 & 0.0 & 0.0 & 0.0 & 5 & 0.0 \\ 0.0 & 0.0 & 0.0 & 5 & 0.0 & 0.0 \\ -1.35 & -1.35 & 3.3 & 0.0 & 0.0 & 0.0 \end{bmatrix} \times 10^{-10} \, \text{M/V} \quad (1)$$

$$\mathbf{C}^{E} = \begin{bmatrix} 8 & 8.4 & 6.8 & 0.0 & 0.0 & 0.0 \\ 8.4 & 8 & 6.8 & 0.0 & 0.0 & 0.0 \\ 6.8 & 6.8 & 6.2 & 0.0 & 0.0 & 0.0 \\ 0.0 & 0.0 & 0.0 & 3.3 & 0.0 & 0.0 \\ 0.0 & 0.0 & 0.0 & 0.0 & 2.8 & 0.0 \\ 0.0 & 0.0 & 0.0 & 0.0 & 0.0 & 2.8 \end{bmatrix} \times 10^{10} \, \text{N/m}^2 \quad (2)$$

$$\boldsymbol{\varepsilon}^{T} = \begin{bmatrix} 8.1 & 0.0 & 0.0 \\ 0.0 & 8.1 & 0.0 \\ 0.0 & 0.0 & 13.7 \end{bmatrix} \times 10^{-9} \, \text{F/m} \quad (3)$$

3 Analysis Design

To generate a 3D elliptical trajectory, the resonance frequencies between the first longitudinal mode and the two directions of the third bending mode must be similar.

Therefore, a conical shape for the horns and back mass was adopted. The conical shape provides an excellent similarity between the longitudinal and two-direction bending modes. Two full set PZT ceramics were used to vibrate the longitudinal motion in the z-direction; the polarity is indicated in Fig. 1b. The longitudinal-vibration mode was excited by the PZT ceramics with no phase difference. The bending-vibration modes were excited by the half PZT ceramics with phase differences of 90° and 180° for the x- and y-axis bending-vibration modes, respectively, as indicated in Fig. 1b.

An analytical model is difficult to develop. Thus, a sensitivity analysis was adopted by adjusting one of the predicted dimensions and analyzing the output modal response. Furthermore, it is difficult to determine the final dimensions of a 3D-UEVT and the coupled natural frequencies of the first longitudinal and two of third bending modes because of the complexity of the transducer shape design. In this study, the final dimensions of the 3D-UEVT structure were determined by a modal simulation using a finite element modeling (FEM) analysis in the SolidWorks Simulation software. A fine standard triangular meshing grid was applied in this study, as shown in the mode shape results (Fig. 2). The meshing element size, total nodes, and total elements were approximately 2.015 mm, 96,553, and 66,150, respectively. A free boundary condition was used. The computing time was approximately 3 min 57 s. In the FEM analysis, the steel plate and tool insert placement were neglected. The steel plate was placed after the zero displacement location determined by the mode shape in blue (see Fig. 2), whereas the red color indicated the maximum displacement. The natural frequencies of the first longitudinal and two directions of the third bending-vibration mode were determined by adjusting
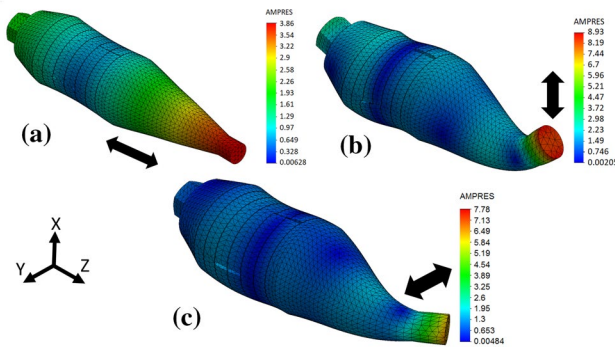
Fig. 2 Three vibrational mode shapes of the 3D-UEVT, **a** 1st longitudinal (Z), **b** 3rd bending (X), and **c** 3rd Bending (Y) [25]

Fig. 3 Structure parameters of 3D-UEVT [25]

the dimensions of the 3D-UEVT structure. First, the working frequency and dimensions of the length of the structure of the 3D-UEVT were defined and calculated. Then, based on the calculated dimensions of the structure, the dimensions of the 3D-UEVT structure were adjusted to determine the coupled working frequencies. Figure 3 displays the dimensions of the 3D-UEVT structure. The longitudinal half-wavelength of the Langevin transducer was adopted to calculate the preliminary dimensions of the structure. The dimensions of the 3D-UEVT, such as L_1, L_2, L_{2-1}, L_{2-2}, L_3, and L_{3-1}, are defined by the following equations.

$$\tan\left(\frac{16\pi f}{c_1}L_1\right) \times tan\left(\frac{16\pi f}{c_0}L_0\right) = \frac{\rho_0 \times c_0 \times A_0}{\rho_1 \times c_1 \times A_1} \tag{4}$$

$$L_2 = \frac{1}{4}\lambda = \frac{1}{4}\frac{c_1}{f} \tag{5}$$

$$L_{2-1} = L_{2-2} = \frac{L_2}{2} \tag{6}$$

$$L_3 = \frac{1}{8}\lambda = \frac{1}{8}\frac{c_2}{f} \tag{7}$$

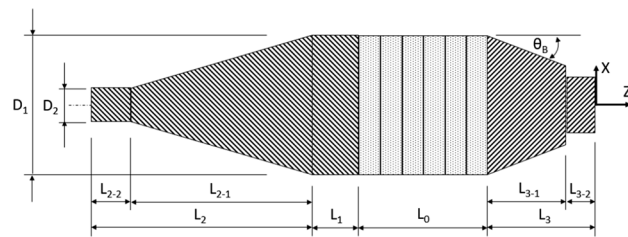$$L_{3-1} = L_3 - L_{3-2} \tag{8}$$

$$c = \sqrt{\frac{E}{\rho}} \tag{9}$$

Parameter c_0 is the sound speed of the PZT ceramic, c_1 is the sound speed of the horn, c_2 is the sound speed of the back mass, and L_0 is the total thickness of six PZT ceramics (30 mm) and seven brass electrodes (1.75 mm). Parameter f is the natural frequency and ρ_0 is the mass density of the PZT ceramic. Parameter ρ_1 is the mass density of the horn. Parameter ρ_2 is the mass density of the back mass and A_0 is the surface area of the PZT ceramic. Parameter A_1 is the surface area of the horn. Equation (9) was used to determine the sound speed. The mass density (ρ) and Young's modulus (E) are listed in Table 1. Equation (4) was used to determine the length of L_1. The parameters L_{2-1} and L_{2-2} are the half-length of L_2, and L_{3-1} is length L_3 minus the length of the head bolt ($L_{3-2}=9.7$ mm). The PZT ceramic had a diameter of 35 mm and a thickness of 5 mm; thus, the diameter D_2 was 35 mm. The diameter D_1 was fixed at 10 mm. The angle θ_B for the back mass was zero for the preliminary dimension structure of the 3D-UEVT. The resonance frequency was set to 25 kHz and the calculated structural parameters of the 3D-UEVT were obtained and are listed in Table 2.

Based on the FEM simulation result after adjusting the dimensions, the coupled working frequencies in the longitudinal–bending–bending mode had similar frequencies. Table 3 lists the final dimensions of the 3D-UEVT after adjusting the dimensions using the FEM modal simulation. Based on the final dimension of the 3D-UEVT (Table 3), the resonance frequency of the first longitudinal-vibration mode in the z-direction was 24,311 Hz. The third

Table 2 Calculated structural parameters of 3D-UEVT in mm [25]

L_0	L_1	L_2	L_{2-1}	L_{2-2}	L_3	L_{3-1}	L_{3-2}	D_1	D_2	θ_B
31.75	5.295	48.69	24.35	24.35	24.37	14.67	9.7	35	10	0°

L_0 = thickness of the PZT and brass electrodes (steel plate thickness was neglected)

Table 3 Final structural parameters of 3D-UEVT in mm

L_0	L_1	L_2	L_{2-1}	L_{2-2}	L_3	L_{3-1}	L_{3-2}	D_1	D_2	θ_B
31.75	5.295	58	49.17	8.83	24.37	14.67	9.7	35	10	21.5°

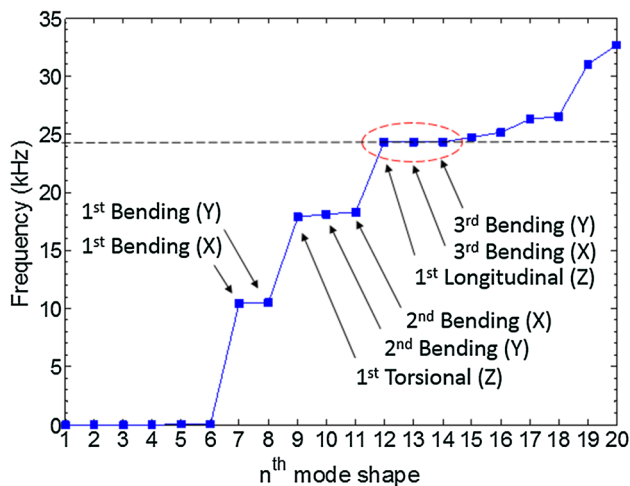L_0 = thickness of the PZT and brass electrodes (steel plate thickness was neglected)

Fig. 4 Natural frequency versus nth mode shape using final structural parameters (Table 3)

Fig. 5 Experimental setup of swept-sine measurement

bending-vibration mode in the x-direction was 24,328 Hz, and the third bending-vibration mode in the y-direction was 24,323 Hz. Figure 4 displays the nth mode shape versus the natural frequency when the coupled working frequencies (longitudinal–bending–bending) were found with the final dimensions listed in Table 3. For the free boundary condition in the modal analysis, the first to the sixth mode shape had a zero natural frequency. Then, the natural frequency gradually increased as the mode shape increased. Similar frequencies, indicated by the red mark in Fig. 4, for the first longitudinal (z-direction), third bending (x-direction), and third bending (y-direction) modes were found. There was no torsional mode shape vibration among these three mode shapes, as indicated in Fig. 4. A detail modal analysis result of the 3D-UEVT, changing the length parameters, was presented in the authors' previous published paper [25].

4 Experimental Dynamic Characteristic

The swept-sine method was used to measure the frequency response function (FRF) of the 3D-UEVT for the longitudinal, bending-x, and bending-y modes. Figure 5 displays the layout of the swept-sine method and the experimental setup during the swept-sine measurement, where the 3D-UEVT was fixed and installed in a 3-axis milling machine. DAQ NI 6251 was used as a function generator as well as a signal analyzer. A monitoring signal was also performed by measuring the generated sinusoidal signal (0 to 10 V) and the output signal from the sensor amplifier (0 to 5 V). The sinusoidal signals were generated continuously in the range 100 Hz to 50 kHz and traveled through the piezo amplifier (0 to 100 V). An optical fiber sensor (Nanotex PM-15) was used to record the displacement during signal excitation.
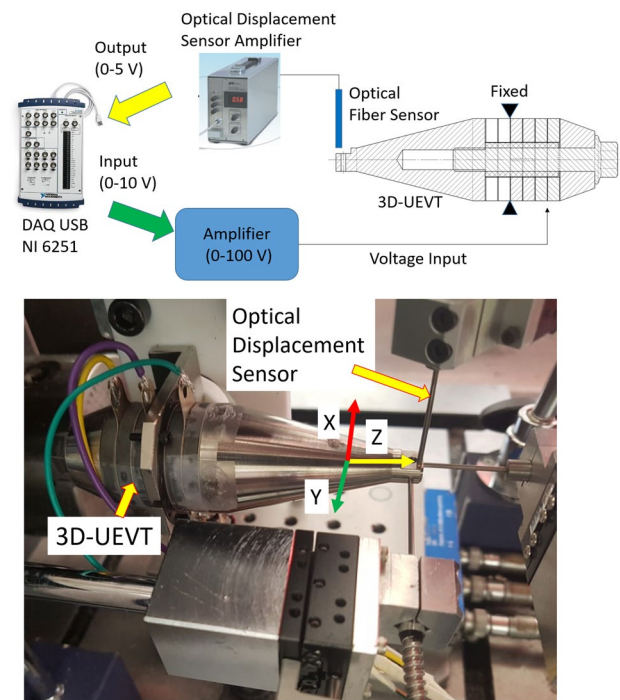

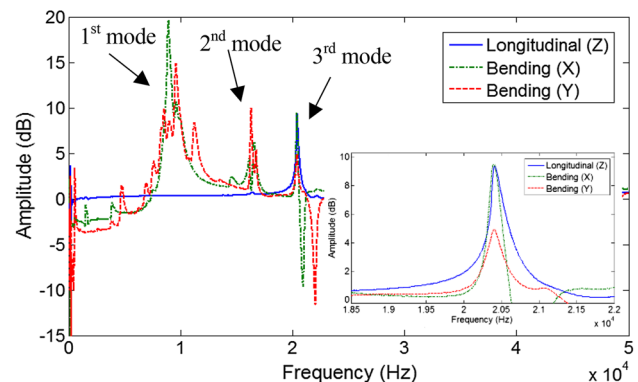**Fig. 6** Frequency response function (FRF) of swept-sine measurement of the 3D-UEVT

The optical fiber sensor had a sensitivity of 12.6 μm/V. The working distance and resolution were 77.6 μm and 39.312 nm, respectively.

Figure 6 displays the results of the swept-sine measurement, where the magnitudes of the longitudinal, bending-x, and bending-y modes are plotted. The first longitudinal mode of the 3D-UEVT had a resonance frequency of approximately 20.4 kHz. The third bending-x and bending-y modes of the 3D-UEVT had resonance frequencies of approximately 20.39 kHz and 20.4 kHz, respectively. These results indicate that the natural frequencies of the longitudinal–bending–bending modes of the 3D-UEVT were equal. Figure 6

Table 4 Summary results of swept-sine measurement

Mode	Longitudinal (Z) (kHz)	Bending (X) (kHz)	Bending (Y) (kHz)
1st	*20.400*	8.924	9.593
2nd	–	16.570	16.320
3rd	–	*20.390*	*20.400*

Italic values indicate the coupled resonance frequencies

Table 5 Summary results of impact hammer test of longitudinal (z-direction), bending-x, and bending-y modes

Mode shape	1st (Hz)	2nd (Hz)	3rd (Hz)
Longitudinal mode	*20,461.6*	–	–
Bending-*x* mode	6640	13,365.33	*20,442.67*
Bending-*y* mode	6853.33	13,712	*20,486.67*

Italic values indicate the coupled resonance frequencies

also indicates that the bending-x and bending-y modes had similar resonance frequencies for the first bending and second bending modes. Table 4 lists the measurement results. When the resonance frequency values between the modal simulation (Fig. 4) and swept-sine method were compared, the resonance frequency values differed. These differences were mainly caused by the differences between the material properties (electrodes properties), boundary condition (fixed or free), meshing model (small or large size), and ideal models [11].

An impact hammer test was also conducted to analyze the resonance frequency of the 3D-UEVT structure. The impact hammer test was performed using an HP 35665A digital signal analyzer, where the excitation signal was provided by a Kistler hammer (9724A model), and the response signal was captured by an accelerometer type 4374 (B & K Instruments). The 3D-UEVT was suspended freely with elastic yarn and it was assumed that there was no effect of external damping.

The impact test for the longitudinal (z-direction), bending-x (x-direction), and bending-y (y-direction) modes were performed. A frequency span from 0 to 25 kHz was used. The resonance frequencies were similar for the longitudinal–bending–bending mode at 20.416 kHz. The average values of the resonance frequencies of the longitudinal, bending-x, and bending-y modes are listed in Table 5.

5 Displacement Prediction and Measurement

Figure 7 displays the three degrees of freedom of the conical horn motion mechanism, where point P was located at the tip of the conical horn. The conical horn was assumed to be pushed vertically by the piezoelectric actuators at five
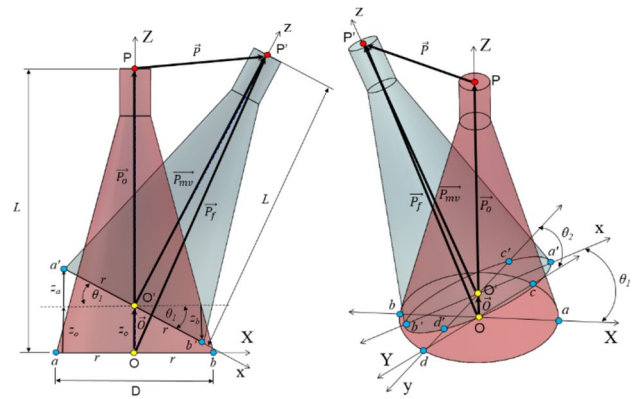

Fig. 7 Three degrees of freedom of conical horn motion mechanism

different points: *a*, *b*, *c*, *d*, and O. Point O is the origin of the fixed frame of the Cartesian coordinate XYZ, and point O′ is the origin of the moving frame of the Cartesian coordinate xyz. The longitudinal piezoelectric actuator vertically pushed point O′, as described by a vector $\vec{O}$. The bending piezoelectric actuators pushed points *a*, *b*, *c*, and *d*. Points *a* and *b* correspond to the bending-*x* piezoelectric actuators, and points *c* and *d* correspond to the bending-*y* piezoelectric actuators. The one-dimensional sinusoidal motion of the piezo electric actuators for the longitudinal (z_o), bending-x (z_a and z_b), and bending-y (z_c and z_d) modes are described by Eq. (10). The z_b and z_d motion was negative or reversed direction because of the reversed polarity of the piezo electric actuator, and the piezo actuator was in the compression state.

$$
\begin{aligned}
z_o &= A_1 \cdot cos\left(2\pi f_m \cdot t + \phi_1\right) \\
z_a &= A_2 \cdot cos\left(2\pi f_m \cdot t + \phi_2\right) \\
z_c &= A_3 \cdot cos\left(2\pi f_m \cdot t + \phi_3\right) \\
z_b &= -z_a \\
z_d &= -z_c
\end{aligned}
\tag{10}
$$

Parameters A_1, A_2, and A_3 are the amplitudes in the z-direction for the longitudinal and bending modes, respectively. Parameter f_m corresponds to the ultrasonic frequency, and t is time. Parameter ϕ is the phase difference between the longitudinal and bending modes, where ϕ_1, ϕ_2, and ϕ_3 are in the range of 0–2π. Assuming A_1, A_2, and A_3 are equal, the amplitude of the piezoelectric actuator is estimated by Eq. (11). Parameter N is the number of piezoelectric actuators and d_{33} is the dielectric coefficient of the piezoelectric actuator (330×10^{-6} μm/V). Parameter $V_{p\text{-}p}$ is the peak-to-peak voltage amplitude and m_f is the multiplication factor due to the resonance state, determined by an amplitude measurement. In this case, $m_f = 1.33$.

$$
A = N \cdot d_{33} \cdot V_{p\text{-}p} \cdot m_f
\tag{11}
$$

According to Fig. 7, the position of points a, b, c, d, and O in the fixed XYZ frame are described by Eq. (12).

$$a = \begin{bmatrix} -r \\ 0 \\ z_a \end{bmatrix}; b = \begin{bmatrix} r \\ 0 \\ z_b \end{bmatrix}; c = \begin{bmatrix} 0 \\ -r \\ z_c \end{bmatrix}; d = \begin{bmatrix} 0 \\ r \\ z_d \end{bmatrix}; O = \begin{bmatrix} 0 \\ 0 \\ 0 \end{bmatrix} \tag{12}$$

Parameter r is the radius of the conical horn, as indicated in Fig. 7. Parameters z_a, z_b, z_c, and z_d are associated with Eq. (10). The positions of the piezo tips a', b', c', d', and O′ in the moving xyz frame are described by Eq. (13).

$$a' = \begin{bmatrix} -r \cdot cos\theta_1 \\ 0 \\ z_a \end{bmatrix}; b' = \begin{bmatrix} r \cdot cos\theta_1 \\ 0 \\ z_b \end{bmatrix};$$

$$c' = \begin{bmatrix} 0 \\ -r \cdot cos\theta_2 \\ z_c \end{bmatrix}; d' = \begin{bmatrix} 0 \\ r \cdot cos\theta_2 \\ z_d \end{bmatrix}; O' = \begin{bmatrix} 0 \\ 0 \\ z_o \end{bmatrix} \tag{13}$$

The parameters θ_1 and θ_2 are the rotational angles along the y- and x-axis direction, respectively. The rotational angles θ_1 and θ_2 were determined by Eq. (14), respectively, due to the pushing mechanism of the piezoelectric actuator. The O′ point moved only in the z-direction about z_o.

$$\theta_1 = sin^{-1}\left(\frac{-z_a}{r}\right); \theta_2 = sin^{-1}\left(\frac{-z_c}{r}\right) \tag{14}$$

Fundamentally, the vector $\vec{P}$ is the main objective to determine the displacement trajectory of point P'. Based on the vector relationship in Fig. 7, $\vec{P}$ is determined by Eq. (15).

$$\vec{P} = \vec{O} + T_R \cdot \overrightarrow{P_{mv}} - \overrightarrow{P_o} \tag{15}$$

Vector $\vec{O}$ is the origin vector of the O′ point of the moving xyz frame with respect to the fixed XYZ frame. The vector $\overrightarrow{P_{mv}}$ has a similar magnitude to vector $\overrightarrow{P_o}$; however, the orientation is based on the moving xyz frame. Vector $\overrightarrow{P_o}$ is a non-moving vector, where the original position of point P is based on the fixed XYZ frame. The parameter T_R is the homogenous transformation matrix that represents the position and orientation of the moving xyz frame with respect to the fixed XYZ frame. The vectors $\overrightarrow{P_o}$, $\overrightarrow{P_{mv}}$, and $\vec{O}$ are determined by Eq. (16), respectively.

$$\overrightarrow{P_o} = \begin{bmatrix} 0 \\ 0 \\ L \\ 1 \end{bmatrix}; \overrightarrow{P_{mv}} = \begin{bmatrix} 0 \\ 0 \\ L \\ 1 \end{bmatrix}; \vec{O} = \begin{bmatrix} 0 \\ 0 \\ z_o \\ 1 \end{bmatrix} \tag{16}$$

The homogeneous transformation matrix is based on the rotation and translation motion mechanisms. Thus, T_R is a function of θ_1, θ_2, and z_o, where the final term of T_R is given by Eq. (17).

$$T_R(\theta_1, \theta_2, z_o) = T(0, 0, z_o) \cdot T(y, \theta_2) \cdot T(x, \theta_1)$$

$$T_R(\theta_1, \theta_2, z_o) = \begin{bmatrix} \cos\theta_2 & \sin\theta_1 \cdot \sin\theta_2 & \cos\theta_1 \cdot \sin\theta_2 & 0 \\ 0 & \cos\theta_1 & -\sin\theta_1 & 0 \\ -\sin\theta_2 & \sin\theta_1 \cdot \cos\theta_2 & \cos\theta_1 \cdot \cos\theta_2 & z_o \\ 0 & 0 & 0 & 1 \end{bmatrix} \tag{17}$$

Figure 8 displays the 3D elliptical trajectory when the phase shift was varied for $\phi_1 = 45°$, $60°$, and $90°$; $\phi_2 = 0°$; and $\phi_3 = 90°$, $120°$, and $180°$, respectively. The excitation voltage was in the square waveform, where the peak-to-peak voltage was approximately 150 V. The vibration frequency of 20.4 kHz was given as the coupling frequency between the longitudinal mode and two-bending modes that were found in the swept-sine and impact test assessments. The 3D-UEVT could generate a peak-to-peak amplitude in the z-direction with an approximate range of 0.3–0.5 μm. The peak-to-peak amplitude for the x- and y-bending was approximately 0.8 μm. The different motion of the elliptical trajectory in the 3D Cartesian space was obtained by changing the phase shift of the driving voltage. The magnitude of the excitation voltage determines the magnitude of the vibration amplitude [11]. The predicted trajectory of the 3D elliptical motion fit adequately with the measurements. Achieving the exact same trajectory was not possible because of hysteresis [26] and the creep of the piezoelectric ceramic actuator.

Figure 9 displays the peak-to-peak displacement of the sinusoidal wave for the x, y, and z-directions when the excitation peak-to-peak voltages were varied from 100 to 220 V. The blue, red, and green lines correspond to the x-, y-, and z-directions, respectively, as indicated in Fig. 9. Figure 9 illustrates that the peak-to-peak displacement for all three directions increased linearly when the excitation voltages increased from 100 to 220 V. Figure 9 also indicates a similar trend for the peak-to-peak displacement of both the experiment and simulation. The maximum peak-to-peak amplitudes obtained experimentally were approximately 1.421, 1.314, and 0.658 μm for the x-, y-, and z-directions, respectively, as displayed in Fig. 9a for the phase 1 $\phi_1 = 45°$, phase 2 $\phi_2 = 0°$, and phase 3 $\phi_3 = 90°$ at a working frequency of 20.4 kHz. Figure 9b, c display the peak-to-peak displacements with voltage variations and different phase shifts. It should be noted that there is a difference between simulation and experiment results in Figs. 8 and 9. The reason might be due to the rigid model assumption in our model. However, the developed transducer vibrates ultrasonically in such a way more flexible manner in the actual condition.
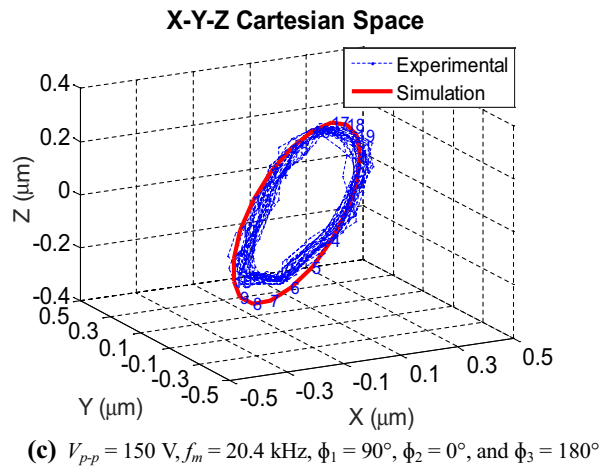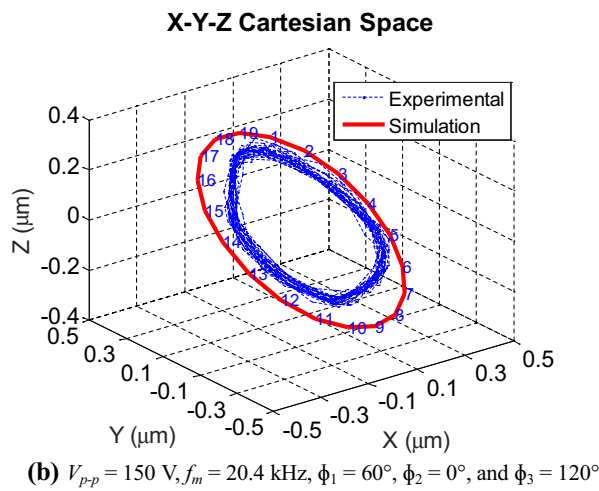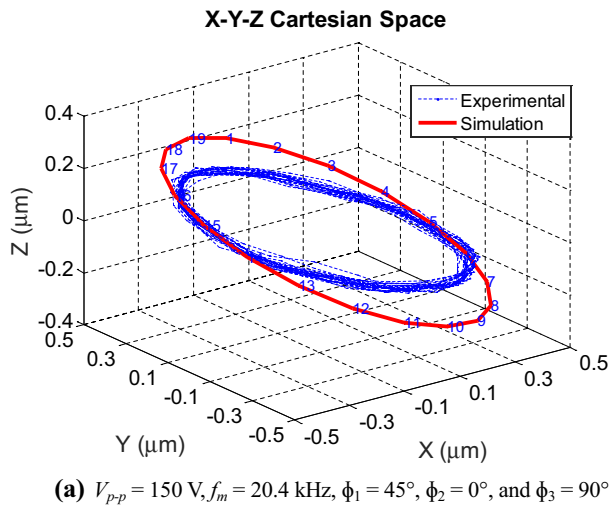
(a) $V_{p\text{-}p}$ = 150 V, f_m = 20.4 kHz, ϕ_1 = 45°, ϕ_2 = 0°, and ϕ_3 = 90°

(b) $V_{p\text{-}p}$ = 150 V, f_m = 20.4 kHz, ϕ_1 = 60°, ϕ_2 = 0°, and ϕ_3 = 120°

(c) $V_{p\text{-}p}$ = 150 V, f_m = 20.4 kHz, ϕ_1 = 90°, ϕ_2 = 0°, and ϕ_3 = 180°

Fig. 8 3D elliptical trajectory of 3D-UEVT in x–y–z Cartesian space

(a) f_m = 20.4 kHz, ϕ_1 = 45°, ϕ_2 = 0°, and ϕ_3 = 90°

(b) f_m = 20.4 kHz, ϕ_1 = 60°, ϕ_2 = 0°, and ϕ_3 = 120°

(c) f_m = 20.4 kHz, ϕ_1 = 90°, ϕ_2 = 0°, and ϕ_3 = 180°

Fig. 9 Displacement measurement with varying driven input voltages

6 Temperature Measurement

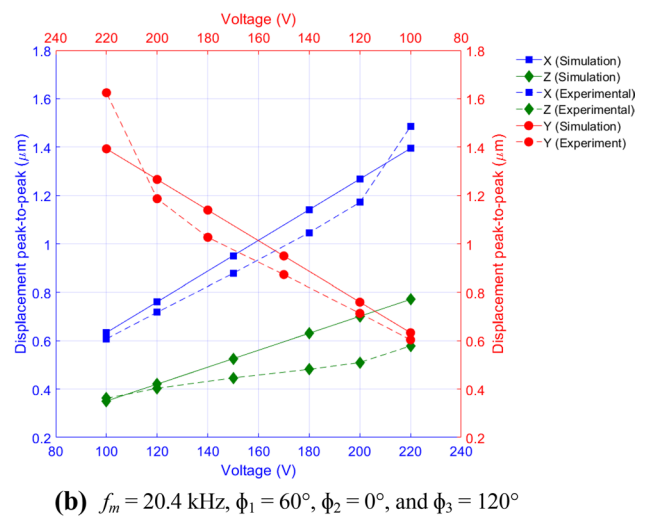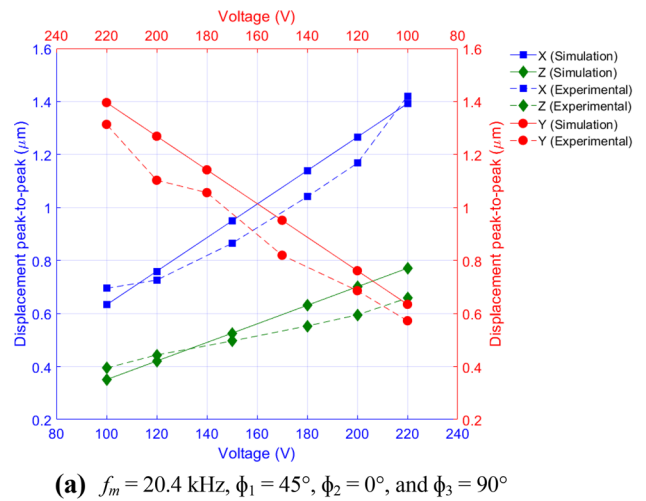The temperature variation of the proposed 3D-UEVT device was performed by locating four type-J thermocouples

at different locations. The four thermocouples used were labeled T1, T2, T3, and T4, located at the conical titanium horn, y-bending half-PZT, longitudinal PZT, and conical

titanium back mass, respectively. A data acquisition Temp-Scan type 1100 was used to capture the temperature data from the type-J thermocouple. A FLIR camera type T335 was also used for the temperature measurement validation and comparison. An emissivity of 0.93 (equal to that of rough fused quartz) [27] was set as a heat radiation parameter constant in the FLIR camera.

Figure 10 displays the temperature rise of the proposed 3D-UEVT driven by different excitation voltage inputs from 120 to 200 V for 30 min. The heat generation of a piezoelectric actuator is typically proportional to the applied electric field [27]. Figure 10 indicates that the temperature increased virtually exponentially as the time increased to 30 min and the temperature achieved a maximum peak.

The maximum temperature of the proposed 3D-UEVT device was observed at the location of T2, with similar results obtained from the FLIR camera. The maximum temperature of the proposed 3D-UEVT device was approximately 42 °C for 30 min at an excitation voltage of 200 V. However, the temperature increase to 42 °C is not significant because the micro-groove process requires no more than approximately 10 min.

7 Micro-grooving Trial

A micro-grooving experiment on a flat surface was conducted to evaluate the feasibility of the proposed 3D-UEVT. Several micro-groove patterns were successfully manufactured on the flat surface of the Al-6061 using the proposed 3D-UEVT device. The micro-grooving process was then performed with a nominal constant cutting speed of 1200 mm/min. The distance between the two micro-grooves was 300 μm, and the nominal depth of the cut was 10 μm. The vibration frequency, phase shifts, and input voltage were maintained constant at $f_m = 20.4$ kHz, $\phi_1 = 45°$, $\phi_2 = 0°$, $\phi_3 = 90°$, and $V_{p-p} = 150$ V. Figure 11 displays the micro-groove comparison results after without and with the 3D-UEVC method that was performed. In general, the ductile cutting regime could be obtained during conventional grooving on a soft work material such as Al-6061. However, Fig. 11a shows micro defects when the conventional grooving was performed. The effect of the micro-brittle grains or micro-hard particles is considered as the reason [28]. Meanwhile, fewer micro defects were obtained when the 3D-UEVC was performed as shown in Fig. 11b. Surface roughness comparison between without and with the 3D-UEVC method is presented in the authors' work [28]. In addition, the SEM results of Fig. 11b indicate that the micro-groove pattern had a uniform roughness morphology and no side-burrs were formed. The micro-groove roughness morphology is dependent on the machining parameters, the hardness of the workpiece, and
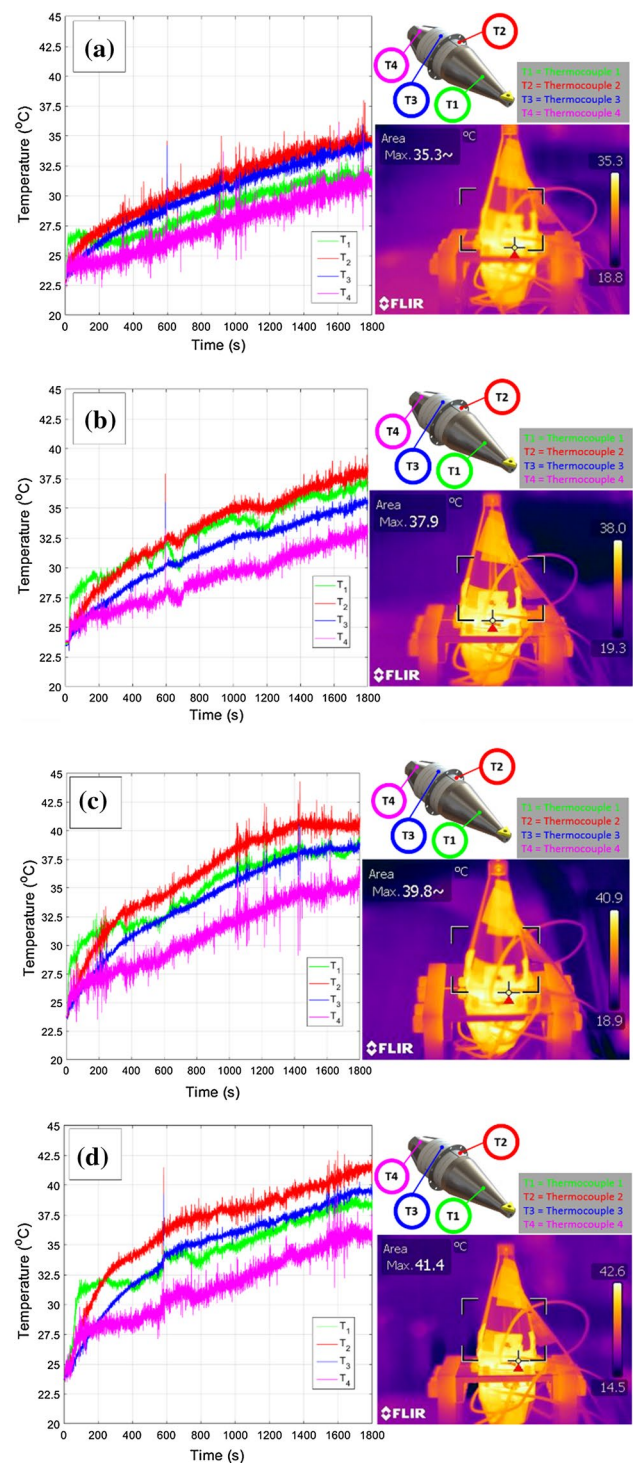

Fig. 10 Temperature increase for different input voltages during operation within 30 min for $f_m = 20.4$ kHz, $\phi_1 = 45°$, $\phi_2 = 0°$, and $\phi_3 = 90°$. **a** $V_{p-p} = 120$ V, **b** $V_{p-p} = 150$ V, **c** $V_{p-p} = 180$ V, and **d** $V_{p-p} = 200$ V

cutting edge quality of the single crystal diamond (SCD) tool [20]. Figure 11c displays the micro-groove 3D profile with an excellent micro-groove morphology using the 3D-UEVC method. The surface morphology of the
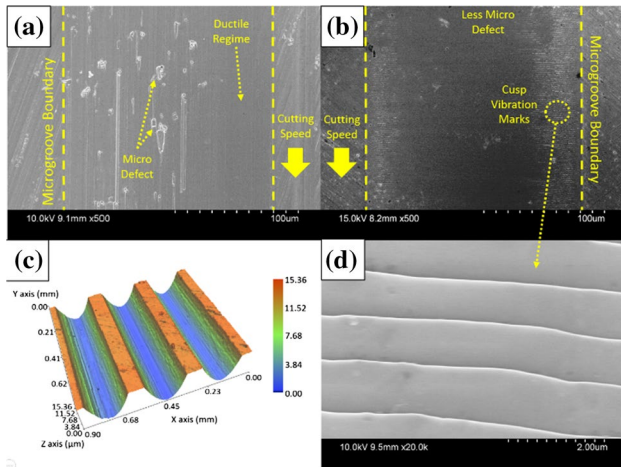
Fig. 11 Micro-groove comparison result after without and with the 3D-UEVC method: **a** without 3D-UEVC, **b** with 3D-UEVC, **c** micro-groove 3D profile, and **d** cusp vibration marks

Fig. 12 SEM image and 3D surface profile of the rhombohedral pattern

micro-groove pattern had cusp vibration marks of approximately 980 nm on average [28], as indicated in Fig. 11d. Because of the effect of the elliptical motion in the 3D Cartesian space, the vibration marks had alignments of 5.5° on average [28], as indicated in Fig. 11d.

A rhombohedral pattern in the form of a micro-pillar pattern was manufactured successfully using the proposed 3D-UEVT. First, the micro-groove was manufactured at a 12 μm depth with a micro-groove distance of 300 μm. Then, the micro-groove was manufactured in a perpendicular manner at an 11 μm depth with a similar micro-groove distance of 300 μm. The rhombohedral pattern had an outstanding micro-pillar profile morphology without burrs on the edge, as indicated in Fig. 12 for both the SEM image and the 3D surface profile. A perfect edge without any damage indicates a less applied cutting load during the micro-grooving process using the proposed 3D-UEVT. Furthermore, the surface roughness of the micro-groove was extremely smooth with an arithmetical roughness value of approximately 140 nm as measured by a non-contact 3D surface profiler Nano System.

8 Conclusion

A novel 3D-UEVT device was proposed and assessed in this study. The 3D-UEVT device operates in the coupling resonant mode of the first longitudinal-vibration mode and the two directions of the third bending-vibration mode. The FEM of the modal analysis was used to determine the coupling resonant frequency and final dimensions of the propo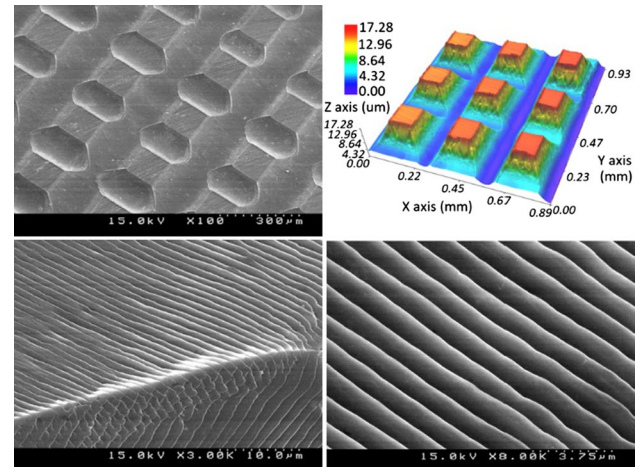sed 3D-UEVT device. A node fixed point was found using the FEM where the steel plate was located to ensure that the node points of the two bending-vibration modes and the longitudinal-vibration mode were in close proximity. Based on experimental assessments, the working frequency of the 3D-UEVT was approximately 20.4 kHz, and the 3D-UEVT could generate a peak-to-peak amplitude of 0.3 to 0.5 μm in the longitudinal direction and 0.8 μm in two-bending directions under an excitation peak-to-peak voltage of 150 V. A micro-groove assessment was performed to evaluate the feasibility of the developed 3D-UEVT device. An acceptable micro-groove pattern morphology was obtained using the 3D-UEVC method with the proposed 3D-UEVT device. Furthermore, an excellent rhombohedral pattern was realized by the proposed 3D-UEVT device. Thus, the proposed 3D-UEVT device is suitable for micro-grooving. A further investigation into the effects of varying the machining parameters will be reported in a future study.

References

1. Shamoto, E., & Moriwaki, T. (1994). Study on elliptical vibration cutting. *CIRP Annals-Manufacturing Technology, 43*(1), 35–38.
2. Jung, H., Hayasaka, T., & Shamoto, E. (2018). Study on process monitoring of elliptical vibration cutting by utilizing internal data in ultrasonic elliptical vibration device. *International Journal of Precision Engineering and Manufacturing Green Technology, 5*(5), 571–581.

3. Guo, P., & Ehmann, K. F. (2013). Development of a tertiary motion generator for elliptical vibration texturing. *Precision Engineering, 37*(2), 364–371.

4. Kim, G. D., & Loh, B. G. (2007). An ultrasonic elliptical vibration cutting device for micro V-groove machining: Kinematical analysis and micro V-groove machining characteristics. *Journal of Materials Processing Technology, 190*(1–3), 181–188.

5. Kurniawan, R., & Ko, T. J. (2014). A new tool holder design with two-dimensional motion for fabricating micro-dimple and groove patterns. *International Journal of Precision Engineering and Manufacturing, 15*(6), 1165–1171.

6. Shi, G., Zhang, C., & Li, Y. (2015). The finite element analysis and optimization of an elliptical vibration assisted cutting device. *Journal of Applied Mechanical Engineering, 4*(4), 170.

7. Li, X., & Zhang, D. (2006). Ultrasonic elliptical vibration transducer driven by single actuator and its application in precision cutting. *Journal of Materials Processing Technology, 180*(1–3), 91–95.

8. Yin, Z., Fu, Y., Xu, J., Li, H., Cao, Z., & Chen, Y. (2017). A novel single driven ultrasonic elliptical vibration cutting device. *International Journal of Advanced Manufacturing Technology, 90*(9–12), 3289–3300.

9. Lin, J., Han, J., Lu, M., Zhou, J., Gu, Y., Jing, X., et al. (2017). Design and performance testing of a novel three-dimensional elliptical vibration turning device. *Micromachines, 8*(10), 305.

10. Zhang, X., & Xu, Q. (2018). Design and testing of a new 3-DOF spatial flexure parallel micropositioning stage. *International Journal of Precision Engineering and Manufacturing, 19*(1), 109–118.

11. Zhou, M., & Hu, L. (2015). Development of an innovative device for ultrasonic elliptical vibration cutting. *Ultrasonics, 60,* 76–81.

12. Huang, W., Yu, D., Zhang, M., Ye, F., & Yao, J. (2017). Analytical design method of a device for ultrasonic elliptical vibration cutting. *Journal of the Acoustic Society of America, 141*(2), 1238–1245.

13. Moriwaki, T., & Shamoto, E. (1995). Ultrasonic elliptical vibration cutting. *CIRP Annals - Manufacturing Technology, 44*(1), 31–34.

14. Kim, G. D., & Loh, B. G. (2010). Machining of micro-channels and pyramid patterns using elliptical vibration cutting. *International Journal of Advanced Manufacturing Technology, 49*(9–12), 961–968.

15. Nath, C., Rahman, M., & Neo, K. S. (2009). A study on ultrasonic elliptical vibration cutting of tungsten carbide. *Journal of Materials Processing Technology, 209*(9), 4459–4464.

16. Kurosawa, M. K., Kodaira, O., Tsuchitoi, Y., & Higuchi, T. (1998). Transducer for high speed and large thrust ultrasonic linear motor using two sandwich-type vibrators. *IEEE Transactions on Ultrasonics, Ferroelectrics, and Frequency Control, 45*(5), 1188–1195.

17. Liu, Y., Shi, S., Li, C., Chen, W., & Liu, J. (2016). A novel standing wave linear piezoelectric actuator using the longitudinal–bending coupling mode. *Sensors and Actuators A: Physical, 251,* 119–125.

18. Liu, Y., Chen, W., Liu, J., & Shi, S. (2010). A cylindrical traveling wave ultrasonic motor using longitudinal and bending composite transducer. *Sensors and Actuators A: Physical, 161*(1–2), 158–163.

19. Yan, J., Liu, Y., Liu, J., Xu, D., & Chen, W. (2016). The design and experiment of a novel ultrasonic motor based on the combination of bending modes. *Ultrasonics, 71,* 205–210.

20. Kurniawan, R., Ko, T. J., Ping, L. C., Thirumalai Kumaran, S., Kiswanto, G., Guo, P., et al. (2017). Development of a two-frequency, elliptical-vibration texturing device for surface texturing. *Journal of Mechanical Science and Technology, 31*(7), 3465–3473.

21. Kurniawan, R., & Ko, T. J. (2019). Cutting force model in micro-dimple pattern process using two-frequency elliptical vibration texturing (TFEVT) method. *International Journal of Precision Engineering and Manufacturing, 20*(1), 1–11.

22. Lotfi, M., & Amini, S. (2018). FE simulation of linear and elliptical ultrasonic vibrations in turning of Inconel 718. *Proceedings of the Institution of Mechanical Engineers, Part E: Journal of Process Mechanical Engineering, 232*(4), 438–448.

23. Lin, J., Lu, M., & Zhou, X. (2016). Development of a non-resonant 3D elliptical vibration cutting apparatus for diamond turning. *Exp. Technical, 40*(1), 173–183.

24. Sajjady, S. A., Abadi, H. N. H., Amini, S., & Nosouhi, R. (2016). Analytical and experimental study of topography of surface texture in ultrasonic vibration assisted turning. *Materials and Design, 93,* 311–323.

25. Kurniawan, R., Ali, S., & Ko, T. J. (2018). Modal simulation analysis of novel 3D elliptical ultrasonic transducer. *IOP Conference Series: Materials Science and Engineering, 324*(1), 012063.

26. Ming, M., Ling, J., Feng, Z., & Xiao, X. (2018). A model prediction control design for inverse multiplicative structure based feedforward hysteresis compensation of a piezo nanopositioning stage. *International Journal of Precision Engineering and Manufacturing, 19*(11), 1699–1708.

27. Zheng, J., Takahashi, S., Yoshikawa, S., & Uchino, K. (1966). Heat generation in multilayer piezoelectric actuators. *Journal of the American Ceramic Society, 79*(12), 3193–3198.

28. Kurniawan, R., & Ko, T. J. (2019). Surface topography analysis in three-dimensional elliptical vibration texturing (3D-EVT). *International Journal of Advanced Manufacturing Technology*. https://doi.org/10.1007/s00170-018-03253-1.

Publisher's Note Springer Nature remains neutral with regard to jurisdictional claims in published maps and institutional affiliations.

Rendi Kurniawan is assistant professor in Mechanical Engineering at Yeungnam University, South Korea. He received Ph.D. degree in mechanical engineering from Yeungnam University, South Korea. His research interests are surface texturing, tribology, friction reduction, micro-dimple fabrication, and elliptical vibration texturing.

Saood Ali is doctoral candidate in Mechanical Engineering at Yeungnam University, South Korea. His research interests are surface texturing, tribology, micro-dimple fabrication, and ultrasonic device.

Chang Ping Li is assistant professor at Hunan University of Science and Technology, China. He received Ph.D. degree in mechanical engineering from Yeungnam University, South Korea. His research interests include ultrasonic device, rotary ultrasonic drilling, and hybrid EDM-milling process.

Ki Moon Park is doctoral candidate in Mechanical Engineering at Yeungnam University, South Korea. His research interests are ultrasonic dental transducer, CFRP drilling, deburring process of CFRP composite, and hybrid deburring process.

Tae Jo Ko is a professor in Mechanical Engineering at Yeungnam University, South Korea. He received Ph.D. in mechanical engineering from POSTECH, South Korea. His research interests include micro-cutting process, non-traditional machining, surface texturing, bio-machining, hybrid EDM-milling process, textured surface on end-mill, deburring process of CFRP composite, CFRP drilling.